Toward the Development of Graphene/Chitosan Biocomposite Aerogels with Enhanced Mechanical and Thermal Insulation Performance

Dang-Thi Le, Benjamin Carbonnier, Séna Hamadi, Daniel Grande, Magali Fois, Salah Naili, Vu-Hieu Nguyen, Samia Mahouche-Chergui

▶ To cite this version:

Dang-Thi Le, Benjamin Carbonnier, Séna Hamadi, Daniel Grande, Magali Fois, et al.. Toward the Development of Graphene/Chitosan Biocomposite Aerogels with Enhanced Mechanical and Thermal Insulation Performance. ACS Applied Polymer Materials, 2024, 6 (21), pp.13132-13146. 10.1021/acsapm.4c02301 . hal-04781870

HAL Id: hal-04781870
https://hal.science/hal-04781870v1

Submitted on 14 Nov 2024

Toward the development of graphene/chitosan biocomposite aerogels with enhanced mechanical and thermal insulation performance

Dang-Thi Le[a,b], Benjamin Carbonnier[a], Séna Hamadi[a], Daniel Grande[a#], Magali Fois[c], Salah Naili[b], Vu-Hieu Nguyen[b], Samia Mahouche-Chergui[a*]

[a]*Univ Paris Est Creteil, CNRS, ICMPE, UMR 7182, 2 rue Henri Dunant, 94320 Thiais, France*
[b]*Univ Paris Est Creteil, Univ Gustave Eiffel, CNRS, UMR 8208, MSME, F-94010 Créteil, France*
[c] *Univ Paris Est Creteil, CERTES, F-94010 Créteil, France*
[#] *Present address: Université de Strasbourg, CNRS, Institut Charles Sadron, UPR 22, 23 rue du Loess, 67034 Strasbourg, France*

[*]E-mail : samia.mahouche-chergui@cnrs.fr

ABSTRACT: Developing lightweight 3D materials from biopolymers that exhibit high heat resistance, improved mechanical strength, and low thermal conductivity is crucial for numerous advanced applications. Herein, we successfully fabricated low-density biocomposite aerogels based on chitosan (CS) with exceptional porous structures (porosity exceeding 98%) by utilizing a straightforward approach free of hazardous chemicals. These aerogels combined high mechanical performance, thermal insulation, thermal stability and fire safety. This was achieved through the incorporation of a small amount of graphene nanofillers (G) using an eco-friendly freeze-drying process. The significant influence of the synthesis method as well as the composition and microstructure on the mechanical and thermal insulation performance of G-CS aerogels were highlighted. Two dispersion approaches for graphene were compared: direct addition to the CS solution followed by sonication, and pre-dispersion in water before incorporation into the CS solution. After multidirectional random freezing at different temperatures (-30°C, -60°C, and -196°C) and subsequent freeze-drying, the second approach yielded superior mechanical properties in G-CS aerogels. These aerogels showed improved mechanical resistance with increasing graphene content, reaching a Young's modulus of 376 KPa, which was 2.75 times larger than that of pure chitosan aerogel. G_{10}-CS showed a remarkable compressive strength to bear loads, approximately 3000 times its weight. SEM analyses revealed that graphene incorporation and reducing the freezing temperature to -60°C transformed the aerogel's microstructure from lamellar to a 3D interconnected honeycomb-like structure, resulting in reduced thermal conductivity (0.038 $W.m^{-1}.K^{-1}$). The G_{10}-CS composite aerogel is expected to be a promising candidate for various practical applications, including thermal and acoustic insulation, energy storage systems, gas detection sensors, biomedical devices, environmental remediation, advanced filtration technologies, and drug delivery.

KEYWORDS: chitosan-based aerogel, graphene, microstructure, robustness, thermal conductivity.

INTRODUCTION

As energy consumption continues to rise and fossil fuels become increasingly scarce, while constituting the main resource of the chemical industry and playing a crucial role as an energy carrier, the significance to find viable solutions to address this growing energy challenge becomes increasingly critical. Thermal insulation materials play a crucial role in minimizing fossil fuel usage and mitigating greenhouse gas emissions across various areas.[1,2] They enable efficient heat management, thereby improving system performance, safety, and durability even in extreme conditions. Moreover, achieving optimal energy efficiency requires the development of lightweight materials with low solid content, which simplifies transportation, installation, and also improves overall thermal regulation. These properties are particularly crucial in advanced technological sectors such as aerospace, automotive, renewable energy, and high-efficiency infrastructure.

Aerogels have emerged as one of the most promising lightweight thermal insulation materials due to their several attractive properties, including ultra-porosity, large surface area, and low thermal conductivity.[3–5] They stand out as a unique class of sol-gel derived solid porous materials, made by extracting liquid from a hydrogel under supercritical conditions and replacing it with air while preserving the original continuous 3D structure as well as the volume of the solid network. [6–14] As a result, aerogels provide significant benefits in minimizing solid heat conduction and restricting thermal convection through their nanoporous network, making them highly effective thermal insulators even in thin layers.

Aerogels can be employed in various sectors. In building construction, they enhance energy efficiency and maintain comfortable indoor temperatures. For example, aerospace applications can benefit from aerogels by reducing weight and enhancing fuel efficiency in spacecraft and satellites. [15,16] Similarly, in automotive manufacturing,[17] aerogels enhance vehicle performance and fuel economy. In electronics,[18] they effectively dissipate heat and prevent overheating. Additionally, they are utilized in food packaging to preserve food quality during transportation and storage.[19] Furthermore, aerogels improve energy storage device performance by increasing capacity and accelerating charge/discharge rates.[20] They also find applications in the military sector,[21] and sports equipment.[22] Despite their numerous advantages, early aerogels exhibit limitations similar to traditional thermal insulation materials, including low mechanical strength, high costs, and varying degrees of toxicity. To provide cost-effective and sustainable solutions that meet diverse application needs, aerogel materials must not only deliver high thermal insulation but also demonstrate robust mechanical performance.[23,24] This dual requirement ensures that aerogels maintain structural integrity during handling, installation, and throughout their operational lifespan as effective lightweight thermal insulation materials. Such durability is crucial for their practical use in real-world environments, promoting long-term energy savings and environmental sustainability objectives.

In this context, carbon-based aerogels,[25] including carbon nanotubes, fullerenes, diamond, graphene and its derivatives, have emerged as promising alternatives to address the challenges associated with traditional silica aerogels as excellent thermal insulation materials.[26–29] Among these, graphene, a single layer of carbon atoms arranged in a two-dimensional honeycomb lattice, stands out due to its outstanding physical properties, including an exceptional surface-to-volume ratio, remarkable mechanical properties, excellent electronic conductivity, high thermal stability, and superior thermal and electrical conductivity.[30,31] Despite its ability to form aerogels through direct crosslinking *via* van der Waals interactions, graphene-based aerogels face drawbacks like weak 3D structures, low mechanical strength under compression, and poor flexibility.[32,33]

A promising method to strengthen the structural integrity of graphene aerogels involves combining graphene with organic polymers to produce graphene-polymer composite aerogels. This approach has been widely validated in the realm of polymer composites.[34,35] Polymers, chosen for their low weight, cost-effectiveness, and high corrosion resistance, serve as ideal matrices for thermal insulation materials. Interestingly, despite graphene high thermal conductivity, graphene-polymer composite aerogels exhibit exceptional thermal insulation capabilities due to their low density and high porosity.[36,37] Substituting non-biodegradable synthetic petroleum-based polymer materials with bio-based polymers derived from renewable sources in the production of graphene composite aerogels is an effective way to fabricate eco-friendly and energy-efficient insulation materials that combine high mechanical strength with low thermal conductivity, aligning with sustainability goals. Chitosan, a natural biopolymer containing amino groups resulting from partial deacetylation of natural chitin, enables the production of highly versatile graphene-chitosan biocomposite aerogels with a unique porous framework. For example, mechanically robust graphene-chitosan aerogels have been successfully prepared and utilized for various applications, such as adsorption in air and water depollution,[38,39] catalysis for hydrogen generation,[40] acting as carriers for pH-responsive drug delivery,[41] functioning as photocatalysts for the degradation of rhodamine B,[42] serving as supercapacitors for energy storage,[43] and acting as hemostatic agents for wound treatment.[44] However, to the best of our knowledge, the thermal conductivity and fire resistance properties of chitosan-graphene aerogels have not been reported so far. Additionally, enhancing mechanical stability while preserving thermal insulation properties without relying on toxic chemical compounds remain a challenge for graphene-based polymer aerogels. In this study, instead of chemically modifying the graphene surface, which involves chemicals, solvents, and complex procedures, or using potentially toxic chemical cross-linkers, we focused on optimizing experimental parameters such as freezing temperature and graphene dispersion. Herein, we detail a straightforward process for fabricating graphene-chitosan biocomposite aerogels, comprising several key steps. This process involves preparing stable graphene suspensions using an ultrasonic tip, with the graphene being slightly oxidized as shown by IR and XPS characterizations. This oxidation enhances the interfacial interaction between the graphene and chitosan. The suspensions are then incorporated into chitosan polymer solutions, followed by molding and freeze-drying. The result is ultralight, thermally stable, fire-safe, and robust solid monolithic aerogels with excellent thermal insulation properties.

MATERIALS AND METHODS

Materials. Graphene nanoplatelets (G, quality level 100: grade C-750, thickness a few nm, particle size <2 μm, bulk density 0.2-0.4 g/cm^3 and surface area 750 m^2/g), chitosan with low molar mass and a deacetylation degree of 75−85 (CS), and glacial acetic acid (AA, ≥ 99.0%) were purchased from Sigma-Aldrich and used without further purification.

Ultrapure water used throughout the experiments was prepared using deionized water (Milli-Q plus purification system, R > 18.2 MΩ cm).

Ultrasonic dispersion of graphene nanoparticles was carried out using BANDELIN SONOPULS HD 3100 homogenizer at a frequency of 20 kHz.

Synthesis of graphene-chitosan biocomposite aerogels (G-CS aerogels). G_x-CS aerogels were prepared using two distinct strategies to disperse varying amounts of graphene nanoparticles (x% weight ratio with respect to the amount of chitosan) while maintaining a constant total concentration of CS in the mixture (2 wt.%). To ensure rigorous comparison the properties of different aerogels, all experiments were conducted using the same batch. The initial step involved dissolving the desired quantity of chitosan powder in 100 mL of acetic acid aqueous solution (1 wt.%) under magnetic stirring at 65°C for approximately 5 h (pH~4.3). In the first strategy, graphene powder was directly added to the CS solution under magnetic stirring, then dispersed *via* ultrasonication for 20 minutes to achieve a homogeneous suspension. The mixture was subsequently kept at room temperature under magnetic stirring for an additional 2 h.

In the second strategy, graphene powder was first dispersed in water *via* ultrasonication for 20 minutes to create a uniform G suspension. The suspension was then added to the pre-prepared CS solution, and the mixture was stirred at room temperature for 2 h.

The resulting suspension was poured into cylinder molds measuring 3.3 cm in diameter and 4 cm in height. These samples underwent random multidirectional freezing inside molds at three different temperatures: -30°C, -60°C (in a freezer), and -196°C (in liquid nitrogen) to study the impact of freezing temperature on the aerogels' structure. Finally, the frozen samples were dried in a freeze-dryer at -105°C and at 0.03 mbar for 48 hours using a Lyovapor L-300 (Buchi, France) to produce chitosan-graphene biocomposite aerogels, designated as G_x-CS. For comparison, a pure CS aerogel was also prepared using the same procedures.

Physico-chemical characterization. The chemical structures of the prepared aerogels were analyzed using Fourier Transform Infrared (FTIR) spectroscopy. Measurements were performed with a Bruker TENSOR 27 FTIR spectrometer in the Attenuated Total Reflectance (ATR) mode. Spectra were recorded within the wavenumber range of 400-4000 cm^{-1} at a resolution of 4 cm^{-1}. Prior to analysis, the samples were dried for at least 1 h in an oven set at 100°C under atmospheric pressure conditions. To ensure consistency for comparison, all spectra were normalized based on the area under the O-C-O vibration band, which appears at around 1020 cm^{-1}.

The surface chemical compositions and surface structure analyses of the biocomposite aerogels were determined employing X-ray Photoelectron Spectroscopy (XPS). A Thermo Scientific K-Alpha spectrometer with a monochromatic Al-Kα X-ray source (hν = 1486 eV) was used, featuring a spot size of 400 µm and pass energy settings of 200 eV for surveys and 50 eV for narrow regions. Data collection and peak fittings in XPS were conducted using Shirley background subtraction with advantage software. Charge compensation was achieved through a combination of an electron flood gun and an argon ion gun. Notably, the high resolution C1s spectra of the G-CS biocomposite aerogels displayed significant C-C and C-H content, which is essential for spectral calibration. The spectra were corrected to a binding energy of 284.8 eV.

The thermal properties of the aerogels were assessed *via* Thermogravimetric Analysis (TGA) using a Setaram Setsys Evolution 16 thermobalance. Approximately 20 mg of each aerogel sample were placed in an aluminum crucible and subjected to heating at a rate of 10°C.min^{-1} within the temperature range of 20 to 800°C under an air flow environment.

The dispersion state of graphene nanoparticles in the biocomposite aerogels was analyzed using X-ray Diffraction (XRD) and transmission electron microscopy (TEM). XRD measurements were conducted on a Bruker D8 Advance diffractometer equipped with a Cu Kα source (λ=1.5418 Å) operating at 45 kV and 44 mA. X-ray diffractograms were obtained from thin disks of aerogels at a scanning rate of 0.2° per minute over a 2θ range from 5 to 60 degrees. The *d* interlayer distance of graphene was calculated using Bragg's equation: $n=2d\sin(\theta)$, where n= 1 and θ is the diffraction angle. TEM analysis was performed with a FEI Tecnai F20 electron microscope operated at 200 kV accelerating voltage. The samples were prepared by dispersing them in absolute ethanol under ultrasonication. The resulting suspension was drop-cast onto a copper grid coated with a Formvar carbon film.

The surface morphology and internal microstructure of the various aerogels were investigated *via* Scanning Electron Microscopy (SEM) using a Zeiss Merlin microscope (Carl Zeiss Company, Germany) equipped with an SE2 detector and operating at an accelerating voltage of 10 kV. Before SEM analysis, the aerogel samples were first cut with a razor, thoroughly dried, and coated with a 5 nm thin layer of Pd for electrical conductivity. Measurements of pore sizes were conducted manually using ImageJ software, with a total of 50 pores analyzed in each SEM image. The evaluation was performed twice in two perpendicular directions for each pore.

Porosity of aerogels. To determine the porosity (P%) of the aerogels, we employed the theoretical method proposed by Sehaqui *et al.* [45], using the following formula:

$$P = \left(1 - \frac{\rho}{\rho s}\right) x\ 100 \qquad (1)$$

where ρ represents the apparent density of the aerogel and ρ_s is the skeletal density. The apparent density (ρ) was determined from $\rho = \frac{\mathrm{m}}{\mathrm{V}}$, where m denotes the mass of the aerogel (g) and V is its volume (cm^3).

The value of ρ_s was estimated based on the bulk density of the components using the following formula[46]:

$$\rho_s = f_{w,G} \times \rho_G + f_{w,CS} \times \rho_{CS} \tag{2}$$

where $f_{w,G}$ *and* $f_{w,CS}$ represent the volume fractions of G and CS, respectively. The bulk densities of G and CS were assumed to be 2.2 $\mathrm{g.cm^{-3}}$ (ρ_G), [47] and 1.4 $\mathrm{g.cm^{-3}}$ (ρ_{CS}), respectively. [48,49]

Rheological measurements. Viscosity measurements of the chitosan solutions were conducted at room temperature using a Discovery HR-2 Rheometer (TA Instruments) equipped with a cone-plate geometry (diameter 20 mm, angle 2°, truncation 53 µm) in the flow mode. The samples were positioned between the parallel plates of the rheometer, maintaining a 1 mm gap. Shear rates ranging from 1 $\mathrm{s^{-1}}$ to 50 $\mathrm{s^{-1}}$ were applied.

Mechanical tests. Uniaxial compressive tests were conducted on cylindrical aerogel samples (diameter ~ 30 mm & height ~ 20 mm) which were positioned between two parallel plates to analyze their mechanical properties. These tests were performed with a universal testing machine (model 5567, Instron, Boston, Massachusetts, America) at room temperature and atmospheric pressure. The aerogel samples were compressed at a displacement rate of 1 $\mathrm{mm.min^{-1}}$ up to 70% of their height using a 2 kN load cell to establish the stress-strain relationship. All compression tests were averaged from three measurements. Young's modulus (E) was estimated as the slope of the stress (σ the physical dimension, which is Pascal) - strain (ε without physical dimension) curves in the linear elastic region at low strain.

It is noteworthy that the absorbed energy was also considered as a key parameter in evaluating of the mechanical properties of the biocomposite aerogels. Specifically, the material absorbs energy when subjected to stress, resulting in deformation in both the elastic and plastic regions. Typically, for aerogel materials, the absorbed energy was calculated in the strain region from 0 to 40%, referred to as $W_{40\%}$, as previously reported.[50] The value of $W_{\varepsilon\%}$ could be easily determined by calculating the area under the stress-strain curve using the following formula:

$$W_{\varepsilon\%} = \int_0^{\varepsilon\%} \sigma d\varepsilon \tag{3}$$

Thermal conductivity measurements. The thermal conductivity values of the aerogels were measured using a Hot-Disk TPS (transient plane source) 2500S thermal analyzer. In the experimental setup, the TPS heater element and temperature sensor were sandwiched between two identical aerogel samples. After a thermal stabilization for 15 min, the aerogel samples were heated with an electrical current generated by the TPS sensor. The time-dependent temperature changes across the samples were accurately recorded, and analyzing this variation (in the transient regime) enabled the determination of thermal conductivity (λ, $W.m^{-1}.K^{-1}$). It is noteworthy that all the thermal conductivity measurements for each sample were conducted in triplicate under ambient temperature and pressure conditions, and an average value was reported. Before the measurements, the samples were dried in an oven at 100°C for 1 h.

RESULTS AND DISCUSSION

Developed strategies for biocomposite aerogels. In this study, as depicted in Scheme 1a, compressible and thermally insulating graphene-chitosan biocomposite aerogels were synthesized using simple and eco-friendly approaches. This involved a liquid dispersion method at pH~4.3, followed by a freeze-drying process. The successful preparation of the G-CS aerogels is attributed to the electrostatic attraction between positively charged moieties in the chitosan polymer and negatively charged groups of graphene, along with hydrogen bonds formed by their hydroxyl and amino/acetamido groups (refer to the proposed interaction mechanism as shown in Scheme 1b). Additionally, intermolecular interactions between chitosan chains, predominantly hydrogen bonds between hydroxyl (OH) groups and between hydroxyl (OH) and amide (CO-NH) groups, further stabilize the composite aerogel structure and enhance its overall integrity. Note that these interactions are responsible for the formation and stability of the 3D structure in pure chitosan aerogels.

The assumption of electrostatic attraction is supported by the zeta-potential results. Specifically, under preparation conditions at pH ~4.3, the zeta-potential data (Scheme 1c) indicated that graphene nanoplatelets carried a negative charge, with a zeta potential of approximately -14 mV, likely due to the deprotonation of carboxylic acid groups. In contrast, CS chains exhibited a positive charge, with a zeta potential of around 58 mV, attributed to the protonation of their amino groups. The first common step involved in both approaches for designing G-CS aerogels was the preparation of chitosan aqueous solution using acetic acid (1%).

In the first approach, graphene powder was directly dispersed into the pre-prepared chitosan solution using ultrasonication. In the second approach, a uniform and stable suspension of graphene nanoplatelets was prepared separately *via* ultrasonication. This suspension was then added to the pre-prepared chitosan aqueous solution under vigorous magnetic stirring at room temperature. It is noteworthy that the final concentration of the CS solution remained identical in both cases. Approaches 1 and 2 were respectively labeled as A1 and A2 in Scheme 1a. The mixtures were then poured into cylindrical polystyrene molds and immediately frozen at different temperatures (-30°C, -60°C, and -196°C). Subsequently, the frozen mixtures were freeze-dried to remove ice, resulting in the preparation of ultralight and flexible sponge-like aerogels.

Scheme 1. (a) Schematic illustration of preparation procedure for G-CS biocomposite aerogels., (b) Schematic representation of the assumed interactions between chitosan (CS) chains and between graphene (G) and chitosan (CS) enabling the generation of G-CS aerogels (c) Zeta potential plots versus pH of G suspension and CS solution from A2 procedure.

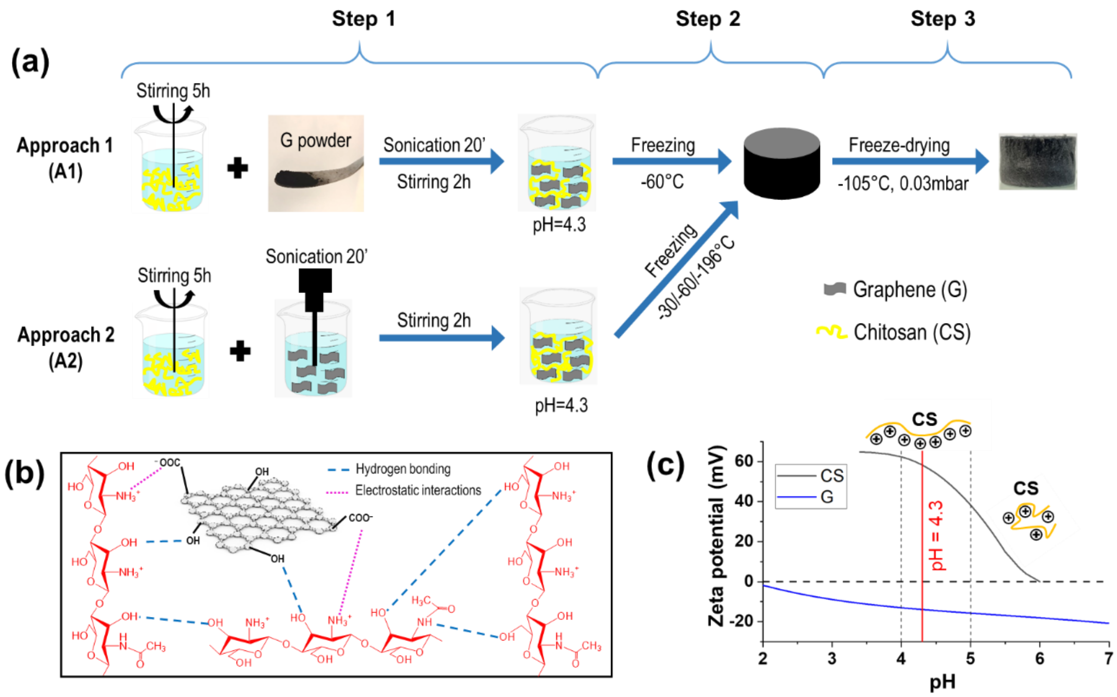

As illustrated in the digital image of Figure 1a, using the G_{10}-CS sample as a representative example, the G-CS composite aerogels were able to hold stably upon a dandelion flower without causing any deformation. This stability could be attributed to their high porosity (~98%), with an ultralow density of 29.0 ± 1.4 $mg.cm^{-3}$.

Moreover, the incorporation of graphene significantly enhanced the compressibility of the composite materials (Figure 1b), preventing the shrinkage observed in pure chitosan aerogels. in preliminary tests, 30 mm-high aerogels were subjected to a 1 kg weight (roughly 2500-3000 times their own weight) for 60 s. The pure chitosan aerogel showed permanent deformation in, whereas the G_{10}-CS biocomposite aerogel regained approximately 95% of its original height immediately after the weight was removed. It is interesting to mention that after a relaxation period of 1 hour, G_5-CS and G_{10}-CS both regained approximately their original height, although slight wrinkles persisted on the G_5-CS sample due to minor deformation. The enhanced robustness and deformability of the CS-based aerogels, despite their low density, could be attributed to the presence of a higher number of physical crosslinks resulting from the strong interactions between chitosan and graphene.

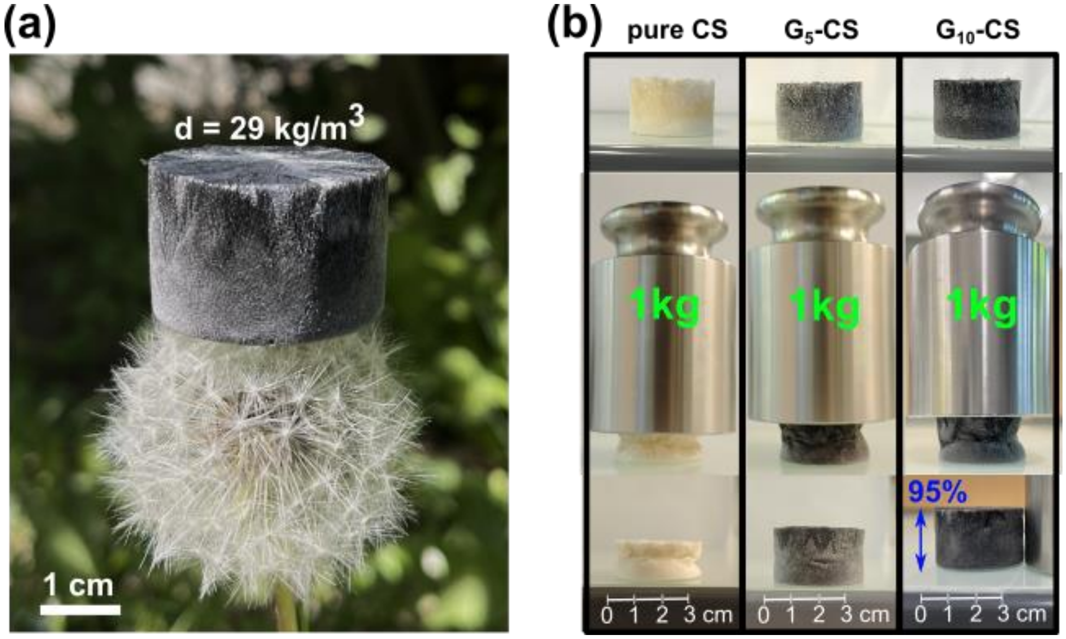

Figure 1. The digital photographs showing (a) the ultralight weight of G$_{10}$-CS aerogel, and (b) the behavior of pure CS, G$_5$-CS and G$_{10}$-CS aerogels supporting 1kg (approximately 3000 times its weight).

Comparison of mechanical properties of aerogels prepared by strategies A1 and A2. Appropriate mechanical properties are crucial for practical use of aerogels as advanced porous materials. Therefore, our study began by investigating the effect of different strategies for dispersing graphene nanoplatelets in chitosan matrix solutions on the mechanical properties (absorbed energy and Young's modulus) of the resulting aerogels, as measured using dynamic axial compression mode. Figure 2a and b illustrate the dynamic vertical compressive stress-strain curves of CS and G$_{10}$-CS (chosen as an example of G-CS aerogel) aerogels prepared at a freezing temperature of -60°C using A1 and A2 strategies, respectively.

Clearly, the curves of both series of aerogels, compressed to 70%, exhibited typical deformation behavior characteristic of polymer-based aerogels, featuring three distinct regions: elastic, plastic, and densification[51] similar to that displayed by 3D honeycomb-like foams. In the elastic region (I), observed at low compressive strain (≤5%), stress increased linearly, and aerogels could recover their original shape reversibly upon stress removal. The plastic region (II), occurring between 5% and 55% compressive strain, witnessed a continuous increase in stress with strain, possibly due to a gradual change in the aerogel structure associated with an irreversible deformation. Furthermore, in the densification region (III) that took place for compressive strain exceeding 55%, stress increased sharply due to aerogel compaction and the collapse of interconnected pore walls, resulting in subsequent structural damage.

The Young's modulus and energy absorption of the aerogels were determined from the slope of the stress-strain curves in the elastic region and up to approximately 40% compressive strain, respectively. It is worth noting that regardless of the dispersion strategy employed for graphene, its addition significantly enhanced the mechanical properties of the aerogels. This enhancement can be attributed to graphene's exceptional strength characteristics (intrinsic strength ~130 GPa and Young's modulus ~1 TPa), combined with its ability to interact with chitosan through both H bonding and electrostatic interactions, thereby forming a reinforced network. When comparing pure CS and G_{10}-CS biocomposite aerogels prepared through A1 and A2 (Figure 2c), it was observed that the aerogels prepared using the latter strategy exhibited superior mechanical strength. Specifically, based on the elastic linear region, Young's modulus of G_{10}-CS obtained from A2 (376 kPa) was found to be 1.35 times larger than that of G_{10}-CS (278 kPa) prepared via A1.

To better understand these results, we examined the rheological properties of two aqueous chitosan solutions (20 mg/mL), one subjected to sonication and the other not. The results (Figure 2d) indicated that both CS solutions exhibited properties characteristic of a Newtonian liquid. Therefore, the Bingham model was used for viscosity calculations. The viscosity of the sonicated CS solution was measured to be equal to 13 mPa.s, representing a five-fold decrease compared to the non-sonicated solution (65 mPa.s). This reduction could be attributed to the decrease in chitosan molecular weight resulting from chains scission induced by ultrasonic waves, as reported in previous studies.[52,53] The breaking of polymer chains results in increased chains mobility, lower chain entanglement and crosslinking densities, thus leading to aerogel materials with lower mechanical performance. Therefore, the second approach was chosen for the preparation of G-CS aerogels subsequently.

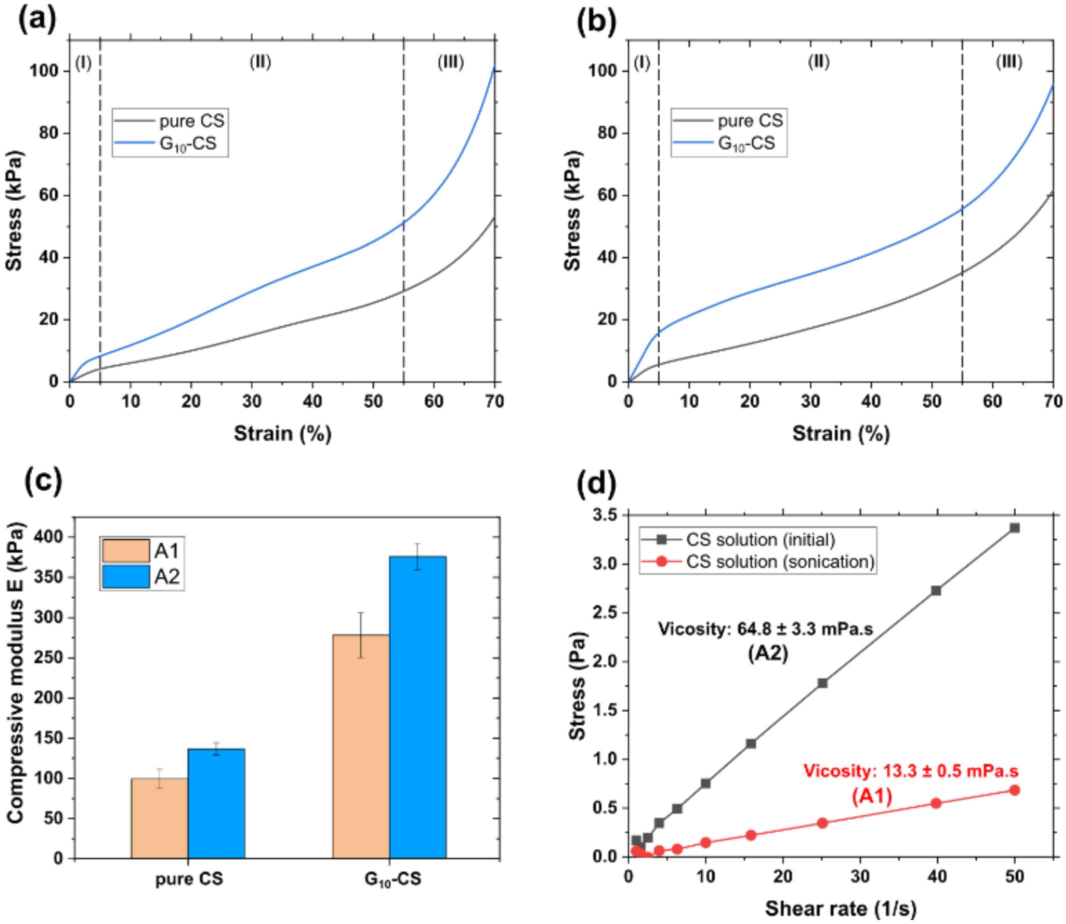

Figure 2. Stress-strain curves of aerogels prepared by (a) A1 and (b) A2 procedures. (c) Comparative histogram representation of the Young's modulus of the different G-CS aerogels prepared following the two approaches. (d) Shear stress versus shear rate data of CS solution before and after ultrasonication.

Structural and morphological characterizations of biocomposite aerogels. The structures of the as-prepared CS and G_{10}-CS aerogels were characterized using FTIR spectroscopy, as illustrated in Figure 3a. The spectrum of the pure CS aerogel revealed characteristic absorption bands, including stretching hydroxyl and amino groups in the 3000-3500 cm^{-1} region, symmetric and asymmetric stretching vibrations of C-H bonds at 2875 cm^{-1} and 2921 cm^{-1}, absorption bands of amide I and OH groups at 1637 cm^{-1}, amide II and protonated amines at 1542 cm^{-1}, bending vibrations of C-H groups at 1398 cm^{-1}, and overlapping stretching vibrations of C-O at 1020 and 1030 cm^{-1}. Additionally, C=O and N-H bending vibrations of amide functions (HN-C(O)-CH_3) related to the acetyl groups arising from N-acetylglucosamine units in chitin were detected at approximately 1637 cm^{-1} and 1542 cm^{-1}, respectively. It is worth noting that the band at 1637 cm^{-1} could also be attributed to the OH groups of chitosan. The spectrum of G_{10}-CS aerogel was very similar to that of pure CS aerogel, with noticeable changes in both the intensities and peak positions in the 3000-3500 cm^{-1} region (NH_2 and OH streching vibrations) and at 1542 cm^{-1} (NH_2 bending vibrations). These findings indicate the formation of intermolecular hydrogen bonds between CS functional groups and the hydrophilic edges of graphene nanoplatelets.

X-ray photoelectron spectroscopy (XPS) was conducted for further characterization of the surface properties and chemical compositions of the aerogels. The survey spectra in Figure 3b revealed the appearance of a characteristic N1s peak at a binding energy of 400 eV in both G_5-CS and G_{10}-CS, in contrast to neat graphene. This peak originated from the incorporation of chitosan, an amine-rich biopolymer. Moreover, chitosan contains oxygen-rich functional groups, which could explain the increase in O/C atomic ratios in G_5-CS (0.78) and G_{10}-CS (0.46) compared to neat graphene (0.07). As graphene content in the aerogels increased, the amount of chitosan decreased. These findings suggested succesful surface modification of graphene by CS chains.

The results were supported by the deconvolution of the C1s spectra, as could be seen in Figure 3c-e. The high-resolution XPS C1s spectra revealed significant differences between neat graphene and G-CS, thus confirming the successful formation of G-CS biocomposite aerogels. The deconvolution of the C1s spectrum of neat graphene could be fitted with five peak components, centered at approximately 284.3, 284.7, 286.7, 287.8 and 290.7 eV, attributed to C=C, C-C/C-H, C-O, O-C=O and the characteristic π-π^* satellite peak from the graphitic carbon atoms, respectively. In contrast, the C1s spectrum of pure CS could be deconvoluted into four peaks at around 285, 285.8, 286.8, and 288.2 eV, attributed to C-C/C-H, C-N, C-O and O-C-O/HN-C=O, respectively. For the G-CS biocomposite aerogels, the deconvolution of the C1s spectrum of G_{10}-CS revealed five main peaks centered at approximately 284.6, 285.8, 286.7, 288.4 and 289.2 eV, assigned to C=C/C-C/C-H, C-N, C-O, O-C-O/HN-C=O and O-C=O, respectively.

Both XPS and FTIR results confirmed the effective self-assembly of graphene and chitosan, involving intermolecular hydrogen bonds between their hydroxyl, amino and acetamido groups as well as electrostatic interactions between protonated amine functions of CS and deprotonated carboxylic acid functions of graphene. Such results are in accordance with the proposed mechanism as depicted in Scheme 1b.

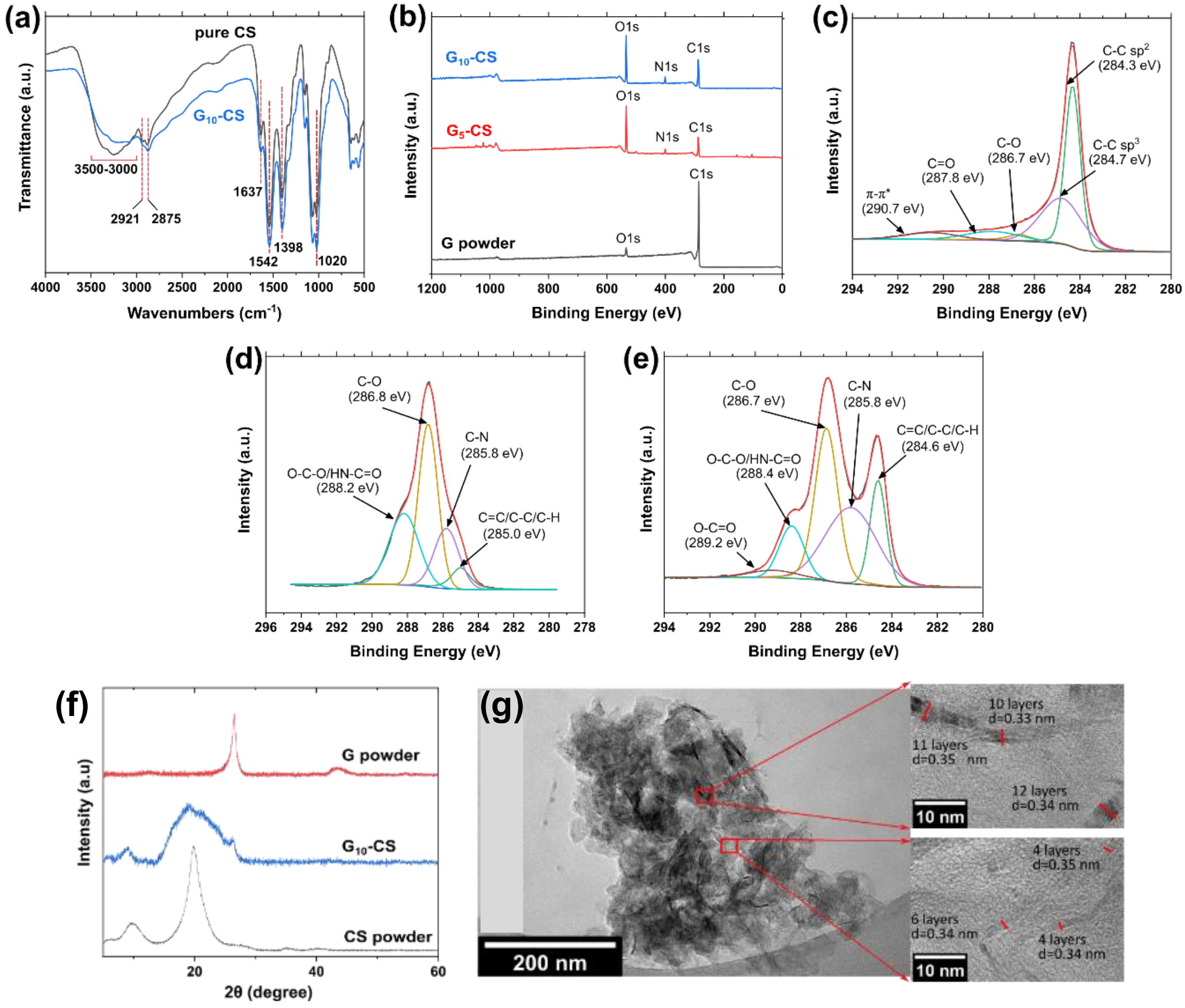

Figure 3. (a) FTIR spectra of pure CS and G_{10}-CS aerogels. (b) XPS survey spectra of GO, G_5-CS and G_{10}-CS aerogels. Deconvolution of high resolution C1s spectra of (c) graphene powder, (d) CS powder, and (e) G_{10}-CS aerogel, (f) XRD patterns of G powder, CS powder, and G_{10}-CS aerogel. (*g*) Typical TEM images of G_{10}-CS aerogel.

The XRD patterns as depicted in Figure 3f compare neat G powder, pure CS, and G_{10}-CS as a representative biocomposite aerogels. In the pattern of G nanoplatelets, a distinct diffraction peak at 26.6° corresponding to the (002) plane of graphitic carbon, indicated a stacked structure of graphene. Calculations based on Bragg's equation revealed a layer-to-layer distance of 0.34 nm, consistent with the structure of graphite. In the pure CS aerogel pattern, two broad peaks were observed around 9° (crystal form I) and 20° (crystal form II), indicative of the semicrystalline structure formed by intermolecular hydrogen bonds. After the incorporation of graphene platelets into the chitosan matrix, these characteristic CS peaks were still observed but appeared wider. Additionally, the intensity of the main peak of graphene decreased, while its position remained unchanged compared to bare graphene (2θ=26.6°). This could be attributed to the low graphene content in the hybrid aerogel, while still maintaining a multilayer graphene structure composed of several overlapping sheets. The driving force behind the layered-stacking structure of graphene was molecular interactions, specifically van der Waals forces and the inter-planar π–π stacking.

To gain a clearer insight into the graphene structure within the G-CS aerogels, we conducted TEM analysis on the G_{10}-CS sample. As depicted in Figure 3g, the graphene nanoplatelets exhibited a tendency to adhere to each other, thus forming agglomerates with 4 to 12 layers per aggregate. Importantly, the interlayer distance between platelets as observed in the TEM images (d = 0.33-0.35 nm) closely matched the values calculated from the XRD data.

The microstructure morphology of G-CS aerogels was investigated using SEM, as shown in Figure 4. Notably, no significant differences were discerned between the cross-sectional and longitudinal views of the aerogels' structure. However, temperature gradients, influenced by the thermal transfer coefficient of the mold, affect the rate of ice crystal formation and, consequently, the structure in different regions of the aerogel (see SEM images a-d from Figure 4). The polystyrene molds used in this study, with their low thermal transfer coefficient, create significant temperature gradients. To enhance heat transfer and reduce these gradients, the polystyrene molds were used without covers, allowing for better control over the direction of ice crystal growth. The schematic representation in Figure 4 shows a pore size gradient within the sample, with smaller pores at the edges and larger pores towards the center, as demonstrated for G_{10}-CS in Figure 4 (images a-d). This variation arises from non-uniform freezing conditions, particularly a temperature gradient. Rapid freezing at the edges promotes faster crystallization, resulting in smaller pores and a honeycomb-like microstructure, while slower freezing at the center allows for the formation of larger pores and a lamellar structure. Similar observations were made under different experimental conditions, such as varying freezing temperatures and graphene content.

We also studied the effect of graphene content on the morphology of various G-CS biocomposite aerogels. Here, we present only the representative cross-sectional images of areas near the edges of the pure CS aerogels and G-CS aerogels with graphene loadings ranging from 2.5 to 15 wt.%. The results revealed that all aerogels exhibited three-dimensional, highly porous structures with notable morphological differences, resulting from the removal of ice crystals through sublimation. This process highlighted the structure of the CS network, characterized by a complex arrangement of pores measuring a few tens of microns, as previously observed by Martina Salzano de Luna and co-workers.[54,55] The pure CS aerogel displayed a parallel arrangement of lamellar structures, with pore sizes ranging from approximately 80 to 250 μm. The lamellae were oriented differently, creating multiple distinct domains. When graphene nanoplatelets were incorporated, a significant morphological transformation occurred. The composite aerogels showed progressive changes with increasing amounts of graphene, developing well-defined, interconnected structures. This suggested that as water started to solidify, combined chitosan molecular chains and graphene platelets were typically excluded from the solid ice phase, forming a layer around the growing ice crystals and resulting in a honeycomb-like microstructure. Additionally, uniformly incorporating graphene into the CS matrix increased its viscosity, thus restricting chain mobility. As a result, the growth of ice crystals was delayed, promoting the formation of numerous small crystals. Upon freeze-drying, this led to an aerogel with an interconnected microporous structure. Furthermore, the G-CS aerogel average pore sizes decreased with increasing graphene contents, reaching a minimum of approximately 76 μm for G_{10}-CS sample. It is noteworthy that when the graphene content exceeded 15 wt.%, the average pore size was found to increase again due to its aggregation within the CS matrix. These morphological changes could be attributed to the increased number of physical interactions between graphene and CS. Specifically, non-covalent crosslinking, implying hydrogen bonding and electrostatic forces between graphene and chitosan, was the primary mechanism driving the formation of the highly interconnected porous structure, enhancing the robustness of these biocomposite aerogels.[56]

However, as illustrated in the histograms in Figure 4 (images e-j), the pore size distribution in the aerogels displayed a relatively broad range that narrowed slightly with the incorporation of up to 10% graphene. This relatively broad distribution could be attributed to the random freezing process used during the aerogel's preparation. The uncontrolled freezing rate and uneven distribution cause the ice crystals to form rapidly and irregularly, leading to varying pore sizes and shapes in the final aerogel. Indeed, one drawback of ice molding is the limited control over the pore size distribution in the final product compared to more precise manufacturing techniques like 3D printing. Despite this, ice molding is valued for its simplicity, uniformity of pore size, and versatility with different materials.

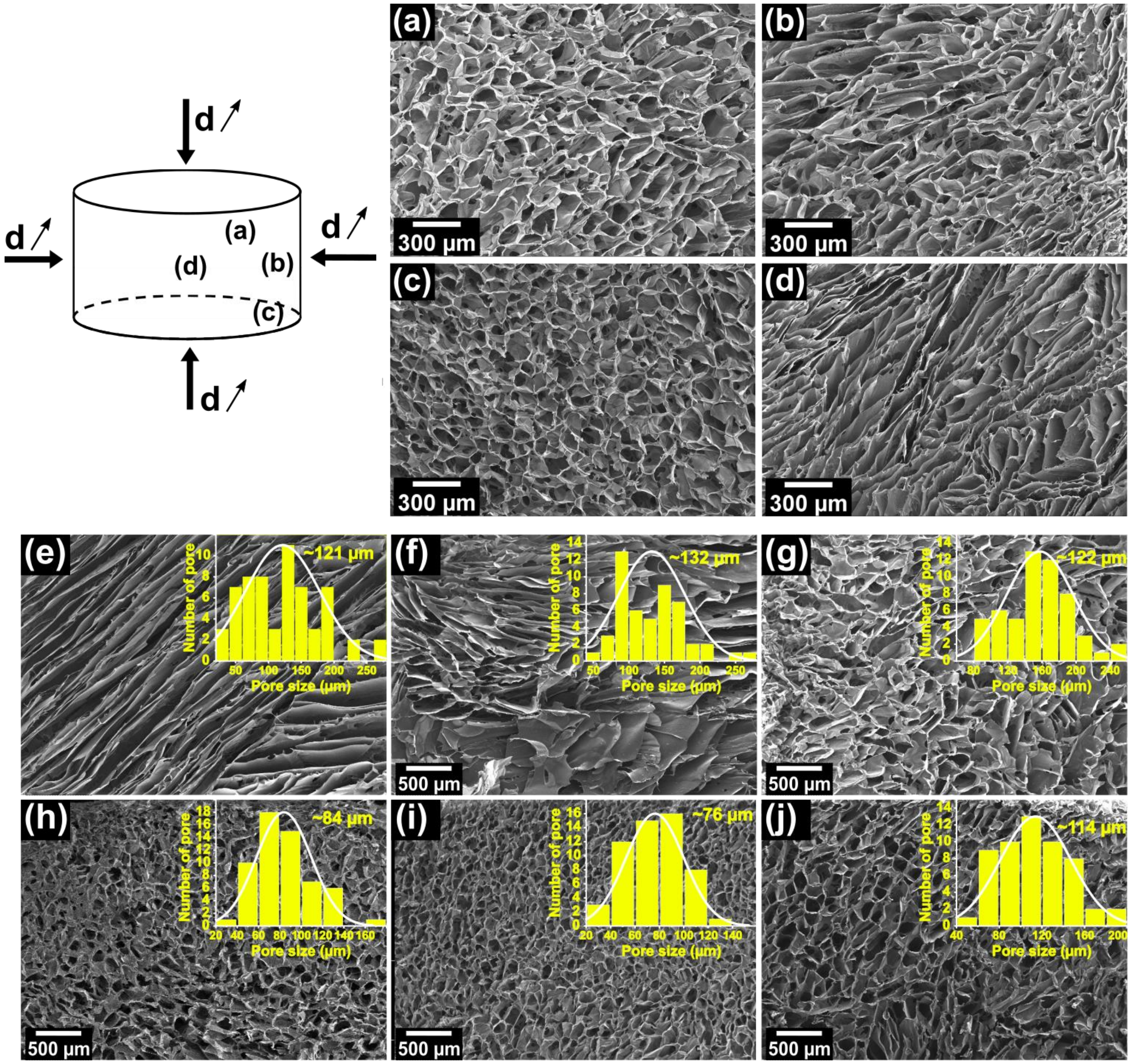

Figure 4. Schematic representation of heat transfer in G-CS biocomposite aerogels prepared in polystyrene mold (d:pore size), SEM images of different areas of the G_{10}-CS aerogel (a-d), SEM images of (e) pure CS aerogel and G-CS aerogels with (f) 2.5 wt.%, (g) 5 wt.%, (h) 7.5 wt.%, (i) 10 wt.%, and (j) 15 wt.% of graphene. The freezing temperature was equal to -60°C.

Effect of graphene nanoplatelets content. To examine how graphene content affected the microstructure, mechanical properties, and thermal conductivity of G-CS biocomposite aerogels, samples with varying amounts of graphene were prepared and analyzed using SEM, uniaxial compression, and Hot-Disk thermal techniques. SEM images as shown in Figures 4 f-j revealed that increasing graphene loadings resulted in more structured interconnected porous networks, leading to smaller pores and narrower pore size distributions, likely due to the formation of additional physical crosslinks. The average pore diameter decreased from 132 µm to 76 µm as graphene content increased from 2.5 wt.% to 10 wt.% but then increased to 114 µm at 15 wt.%. This structural change highlighted by SEM after graphene addition had a significant impact on macroscopic performance.

As anticipated, the addition of graphene nanoplatelets substantially enhanced the mechanical integrity (Young's modulus and energy absorption, Figure 5a) of the G-CS aerogels. For example, incorporation of 2.5 wt.%, and 10 wt.% of graphene in the CS-based aerogels gradually increased the Young's modulus from 137 to 200 and 376 kPa, corresponding to 46% and 174% increases, respectively, as compared to neat CS. However, it was noteworthy that the reinforcement effect decreased when the amount of incorporated graphene increased to 15 wt.%. While remaining significantly higher than that of the 2.5 wt.% and 5 wt.% loadings. This was likely due to the reduced dispersion of graphene nanoplatelets which may form aggregates, thus decreased interactions with CS chains.[57, 58] A similar phenomenon was observed in our previous work with nanofillers of a different nature, namely clay.[59]

Thermal insulation plays a crucial role as an initial step towards a more sustainable and energy-efficient future across various applications, including transportation, manufacturing, and energy storage systems. To further explore the thermal insulation behavior of G-CS biocomposite aerogels, the Hot-Disk method was employed to measure their thermal conductivity and assess the impact of graphene content. The findings are summarized in Figure 5b.

Considering the heat transfer mechanisms in aerogels, the effective thermal conductivity comprises solid thermal conductivity, gas thermal conductivity and radiative thermal conductivity ($\lambda_{total} = \lambda_s + \lambda_g + \lambda_r$). The solid thermal conductivity ($\lambda_{sol} = 1/3 \int C_v \rho v l$), depends on the density of the aerogel and the material's nature. For the material, a higher density results in increased solid thermal conductivity. Gas thermal conductivity (λ_{gas}, air), affected by pore size, decreases as pores become smaller because smaller pores restrict the movement of gas molecules, thus reducing λ_{gas}. When pore sizes fall below the mean free path of air molecules (~70 nm), λ_{gas} can approach zero due to the Knudsen effect, wherein collisions between gas molecules and solid surfaces become predominant. Radiative thermal conductivity (λ_{rad}) is generally negligible in optically thick materials, such as carbon-based aerogels, which effectively absorb infrared radiation. Therefore, the overall thermal conductivity of aerogels is determined by the combination of these contributions, with pore structure, density, and the material nature playing key roles. In conclusion, for making effective insulation materials, it is needed to have a compromise between low density and small pores.

From the thermal conductivity results as illustrated in Figure 5b, it could be noted that incorporation of small amounts of G below 5 wt.% did not affect the thermal conductivity of the biocomposite aerogels which remained almost identical to that of pure CS aerogel. This could be explained by the fact that at low concentrations, graphene does not significantly alter the pore structure or density of the aerogels as shown by the SEM images in Figure 4b-c. As a result, the properties of the biocomposite aerogel are primarily dictated by the chitosan matrix. Moreover, the results show that increasing the graphene content from 5 to 10 wt.% in G-CS biocomposite aerogels gradually reduced thermal conductivity, reaching as low as 0.038 $W.m^{-1}.K^{-1}$ for G_{10}-CS. This reduction can be attributed to the decrease in pore size, which limits gas transmission and thus lowers gaseous thermal conductivity, in accordance with the Knudsen effect. While it is generally expected that an increase in density would lead to higher solid-state thermal conductivity, the density of the G-CS aerogels exhibited only a slight increase (see Figure 5b), which limited this effect. Consequently, the reduction in gaseous thermal conductivity could counterbalance any potential increase in solid-state conductivity, leading to an overall decrease in thermal conductivity. The thermal insulation properties of G-CS aerogels are closely related to their pore structures, where smaller pores enhance thermal insulation by reducing gas transmission. Notably, at the optimal graphene content of 10 wt.%, the mechanical performance of the biocomposite aerogels significantly improved while still maintaining low thermal conductivity.

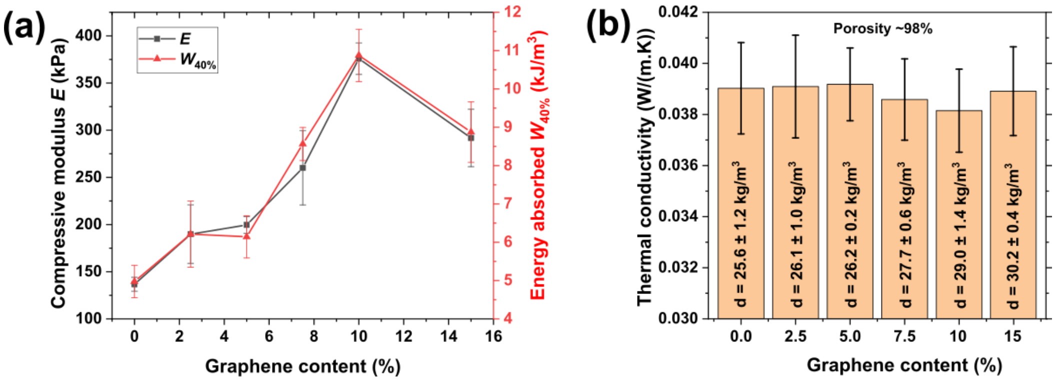

Figure 5. (a) Young's modulus and energy absorbed W_{40}%. (b) Comparative histogram representation of the thermal conductivity of G-CS aerogels, prepared at freezing temperatures of -60°C, with different G contents.

Effect of freezing temperature. As previously mentioned, the porous network of the aerogels resulted from the hypercritical evacuation of ice crystals formed during the freezing process, indicating that this step significantly influenced the aerogel microstructure. The freezing process, including both the cooling rate (reflected in freezing time) and temperature, may markedly affect water crystallization and subsequent ice crystal growth, thus playing a crucial role in determining pore size, shape, and distribution within the three-dimensional aerogel network structure.

To investigate this phenomenon, we examined the effect of three freezing temperatures (-30°C, -60°C, and -196°C) on the performance of G_{10}-CS aerogels. These temperatures were achieved using a conventional refrigerator freezer compartment, an ultralow temperature freezer, and liquid nitrogen, respectively. These varying temperatures induced different freezing rates and, consequently, lead to different nucleation and growth of ice crystals.

The morphology and microstructure of the G_{10}-CS aerogel prepared at different freezing temperatures were characterized using SEM. Figure 6 presents typical SEM images (a, b, and c) alongside magnified SEM images (e, f, and g). Both aerogels prepared at -30°C and -60°C exhibited extremely porous networks with very similar densities (~29.6 ± 0.5 kg/m^3 and 29.0 ± 1.4 kg/m^3, respectively). Nevertheless, a significant difference in pore shape and size was observed because of varying morphology and sizes of ice crystals. The aerogel produced at -30°C exhibited a random structure with long and narrow pores (~241 × 93 μm^2), while a more uniform porous structure with smaller honeycomb-like pores (~76 μm) was observed for the aerogel produced at -60°C. The phenomenon could be explained by the decrease in the time required for ice crystal growth at lower freezing temperatures, resulting in smaller and more compact crystals and thus the formation of finer structures. Conversely, at higher temperatures, water molecules possess greater kinetic energy, which generally promotes faster growth of ice crystals, leading in the formation of larger crystals that create larger pore sizes and lamellar structures.[60] Freezing in liquid nitrogen, at very low temperatures, promoted the formation of lamellar-shaped pores due to an extremely rapid and uniform freezing process. Indeed, water molecules froze instantaneously, and ice crystals develop uniformly in all directions, creating a lamellar porous structure with closely arranged lamellae. As illustrated in Figure 6g, this process resulted in a very small interlamellar distance of approximately 11 μm, contributing to an increase in the density of the porous network to approximately 41.4 mg/cm^3. Therefore, producing aerogels at extremely low temperatures may not be advantageous in terms of achieving a highly porous material with a low density. Furthermore, the aerogels prepared under this temperature exhibited significant damage, as illustrated in Figure 6d. Numerous structural cracks (as indicated by arrows) were observed, likely induced by thermal shocks, rendering the aerogel unsuitable for further use. These cracks were a critical limiting factor in the mechanical strength of materials. The changes in the aerogels' microstructure, associated with different freezing temperatures, play a decisive role in determining their macroscopic properties, such as mechanical and thermal insulation performance.

Based on the inset of Figure 6, which displays the bulk density and porosity of the prepared graphene-chitosan aerogels, the decrease in the freezing temperature resulted in an increase in the calculated apparent densities of the aerogels, from 29.6 to 41.4 $mg.\ cm^{-3}$. Consequently, as porosity was inversely proportional to apparent density, the porosity decreased from 98.0 % for G_{10}-CS prepared at -30°C to 97.3 % for G_{10}-CS prepared as prepared at -196°C. It could be seen from Figure 6i that the biocomposite aerogel as prepared at -60°C exhibited a more pronounced linear elastic region than the aerogel as prepared at -30°C achieving a higher Young's modulus of approximately 376 kPa (Figure 6j). This improvement could be related to *(i)* the much more uniform network structure and *(ii)* the well-organized pore walls of the aerogel as prepared at -60°C as shown by SEM images. Decreasing the freezing temperature of aerogels from -30 to -60°C induced a remarkable change in the pore structure forming smaller pores at -60°C. As a result, the G_{10}-CS biocomposite aerogel prepared at -60°C exhibited superior thermal insulation performance than that prepared at -30°C, decreasing by 16.5% the thermal conductivity (Figure 6k). When the freezing temperature was equal to -60°C, both mechanical strength and thermal insulation performances of G_{10}-CS reached a maximum.

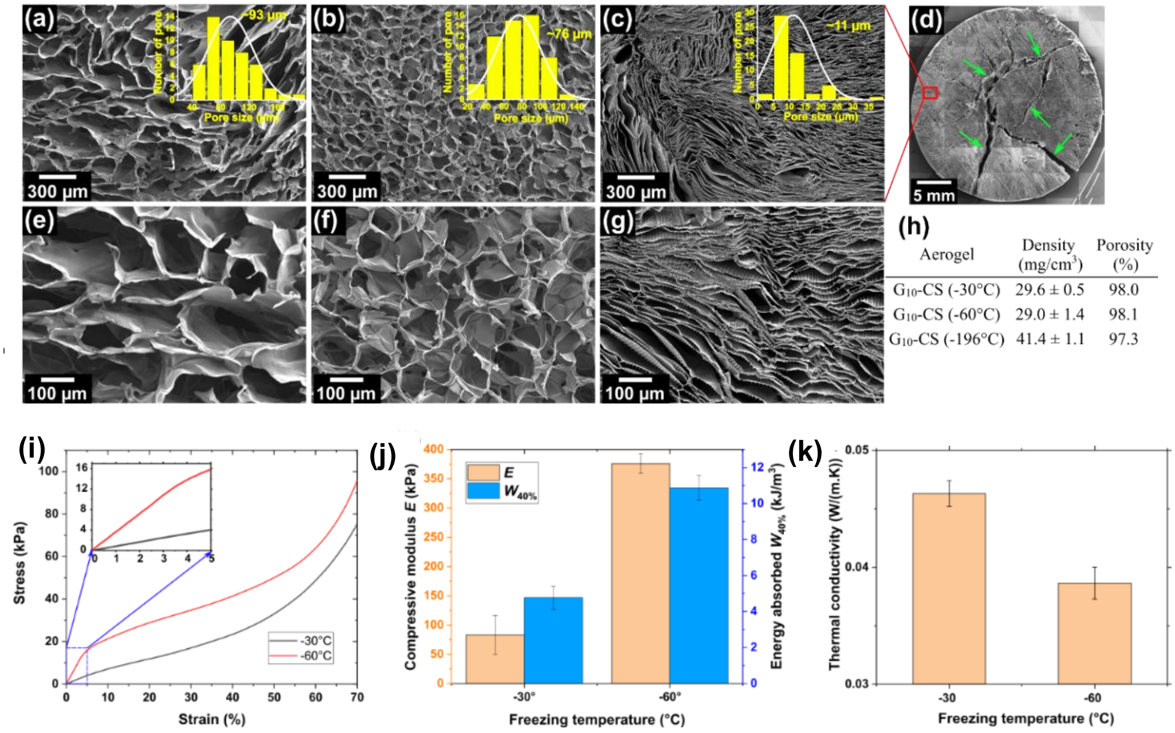

Aerogel	Density (mg/cm^3)	Porosity (%)
G_{10}-CS (-30°C)	29.6 ± 0.5	98.0
G_{10}-CS (-60°C)	29.0 ± 1.4	98.1
G_{10}-CS (-196°C)	41.4 ± 1.1	97.3

Figure 6. SEM images of G_{10}-CS prepared at freezing temperatures of -30°C (a, e), -60°C (b, f), and -196°C (c, g), accompanied by a digital photo of G_{10}-CS prepared at -196°C (d). Arrows indicate the appearance of cracks. (h) Apparent density and porosity data are indicated for the aerogels. A comparative histogram representation of the (*i*) stress-strain curves (*j*) Young's modulus and energy absorbed W_{40}% (*k*) thermal conductivity of G_{10}-CS aerogels prepared at freezing temperature of -30°C and -60°C.

Table 1. Comparison of density, Young's modulus, and specific modulus values of chitosan/graphene-based aerogels for present investigation and available data in the literature.

Aerogel[a]	**Density ρ kg/m^3**	**Young's modulus E kPa**	**Specific modulus E^* kPa/(kg/m^3)**	**Reference**
G_{10}-CS (-60°C)	29.0	376	12.97	Present work
CS5/GO1	4.178	2.107	0.50	51
CS10/GO1	7.523	7.931	1.05	51
CS20/GO1	13.87	91.89	6.63	51
CS40/GO1	24.53	229.7	9.36	51
RGSA-15	10.8	22.5	2.08	61
rGO/CS20	9.3	26	2.79	62
MCG_5A	5.9	1.7	0.29	63

[a] RGSA: reduced graphene oxide-chitosan aerogels and MCG_5A: modified cellulose-graphene aerogels.

Table 1 compares the results of this study with existing literature on graphene derivative-chitosan aerogels. Since density significantly affects the Young's modulus of aerogels, to accurately compare their mechanical properties, the specific modulus E* was calculated by dividing the Young's modulus E by the density ρ (E* = E/ρ). It was obvious that the calculated value for E* of G_{10}-CS aerogel in this study revealed significantly superior mechanical performance compared to the reported data in the literature. This demonstrated the effectiveness of our optimized experimental protocol in the fabrication of graphene-based polymer composite aerogels.

Thermal stability of aerogels. The thermal stability of pure CS, G_5-CS, G_{10}-CS aerogels and G powder was investigated by TGA from room temperature to 800°C. The respective curves are depicted in Figures 7 a-b. Chitosan exhibits a high affinity toward water due to the hydroxyl and amino groups present in its molecular structure, a common characteristic among biopolymer-based materials. The initial mass loss, primarily attributed to the desorption of water (4 wt.%), was noticeable at temperatures below 150°C. Subsequently, the pure chitosan aerogel underwent two stages of decomposition. The first stage occurred between 180°C and 325°C, where a mass loss of approximately 51 wt.%, attributed to the removal of hydroxyl, amino, and acetamido functional groups in CS. The second stage between 325°C and 600°C involved the decomposition of polymer chains, resulting in an additional mass loss of approximately 42 wt.%. In the G_5-CS and G_{10}-CS aerogel samples, the initial decomposition stage between 180°C and 325°C closely resembled that of pure CS aerogels. However, during the second stage, occurring between 325°C and 600°C, an additional phase arose between 540°C and 600°C, indicating the combustion of graphene within the aerogels. The mass loss values for the G_5-CS and G_{10}-CS aerogels between 325°C and 600°C were equal to 43.5 wt.% and 42 wt.%, respectively. In contrast, G powder underwent a single decomposition stage, leading to a 87 wt.% mass loss at the end of combustion at 720°C. The residues of CS, G_5-CS, and G_{10}-CS aerogels at 600°C were equal to 3 wt.%, 4.6 wt.% and 8.8%, respectively. The incorporation of graphene platelets in the CS-based aerogels enhanced the carbon yield. Consequently, the presence of graphene retarded mass loss and inhibited additional thermal decomposition of CS during combustion.

Table 2. Comparison of density, thermal conductivity, and thermal stability values of chitosan/graphene-based aerogels for present investigation and available data in the literature.

Aerogel[a]	**Density ρ (kg/m^3)**	**Thermal conductivity λ (W.m^{-1}.K^{-1})**	**Thermal Stability (°C)**	**Reference**
G_{10}-CS (-60°C)	29	0.038	~220	Present work
CNF/CS 4	19.6	0.036	~280	[64]
CNF/MMT/CS	20.2	0.048	~200-300	[65]
CCA2	16	0.038	~250	[66]
ATP/PDA/GA (2)	62	0.035	400	[67]
G/CS/agar	3.1	0.052	-	[68]
G/ECNCs/CS/agar	3.2	0.045	-	[68]
ETT-20-SF-15	170	0.039	~300	[69]

[a] G: graphene, CNF: cellulose nanofiber, CS: chitosan, MMT: clay, CCA: chitosan/montmorillonite/carbon nanotube, ATP: attapulgite, PDA: polydopamine, GA: gelatin, ECNCs: esterified cellulose nanocrystals, ETT: silica, SF: silk fibroin.

As shown in Table 2, the G_{10}-CS biocomposite aerogel exhibits thermal stability and insulation performance comparable to previously reported biopolymer-reinforced aerogels. Its thermal conductivity is similar to that of conventional biobased materials, such as wood, cellulose, and hemp fiber insulation, which typically range around 0.04 W/m.K. Furthermore, it demonstrates competitive thermal conductivity relative to other widely used insulation materials, including wool (λ ~ 0.030 to 0.040 W/m·K), expanded polystyrene (λ ~ 0.035 to 0.038 W/m.K), and rock wool (λ ~ 0.033 to 0.045 W/m.K).[70]

Evaluation of fire retardancy associated with aerogels. The flame retardancy properties of aerogels are greatly desired due to their potential applications across various industries. In this study, we evaluated the flammability and the combustion behavior of the prepared aerogels by exposing them directly to the flame of a Bunsen burner (vertical burning test, UL-94). As observed in Figure 7c, the loss of the original shape (specifically the diameter) of the G_{10}-CS composite aerogel was less pronounced than that of the pure CS aerogel. The addition of graphene likely contributed to maintaining the aerogel framework during combustion. Furthermore, both samples exhibited slow and incomplete combustion. The analysis of mass loss following exposure to fire for various durations revealed that the addition of graphene to the aerogel matrix slightly enhanced its flame resistance properties, as evidenced by the difference in mass loss (Figure 7d). For example, after 1, 2, and 3 min of exposure to fire, the pure CS aerogel retained only 19.8%, 18.3%, and 17.4% of its mass, respectively. In contrast, the G_{10}-CS aerogel demonstrated higher remaining mass percentages of 28.4%, 26.2%, and 24.2% for the same durations. These results highlighted the effectiveness of graphene in improving the fire resistance of aerogels. Such flame-retardant characteristics are critical for enhancing the safety and durability of materials in applications where fire resistance is essential.

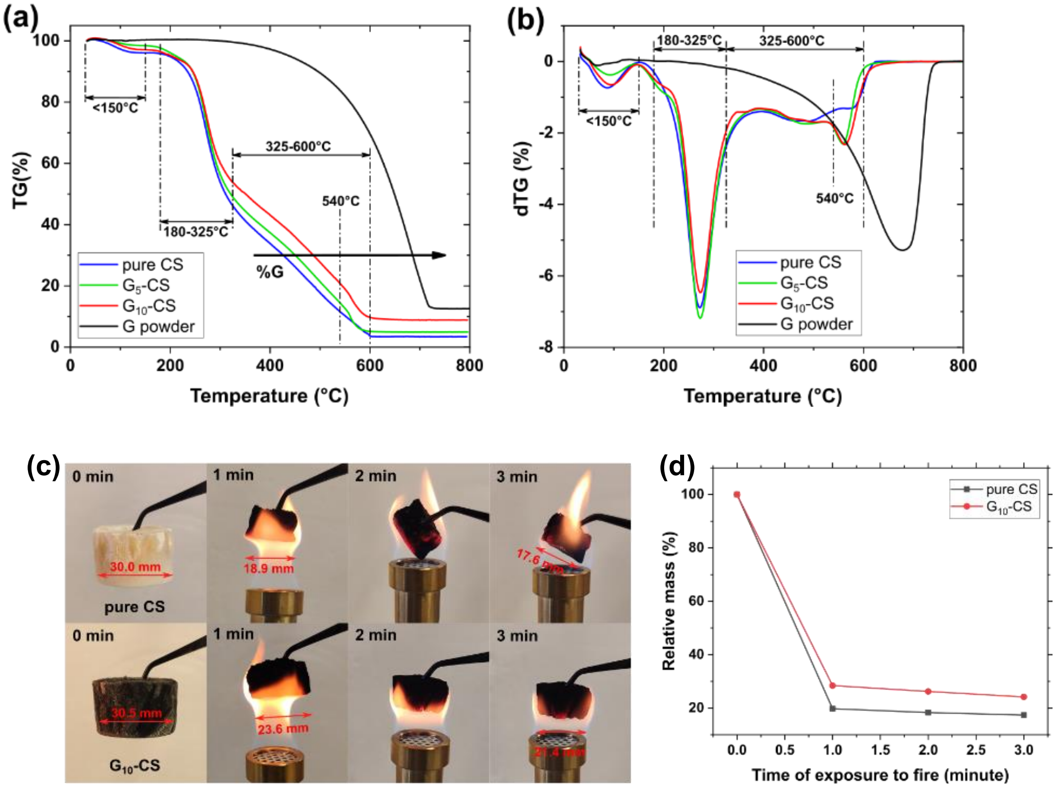

Figure 7. (a) TGA and (b) dTG curves of graphene powder and pure CS, G_5-CS, G_{10}-CS aerogels, prepared at freezing temperature of -60°C, (c) Video screenshots showing combustion behaviors of (Top) pure CS and (Bottom) G_{10}-CS aerogels, prepared at freezing temperature of -60°C and (d) curves of relative mass of pure CS and G_{10}-CS aerogels at different combustion times.

CONCLUSIONS

The objective of cost-effective development of high-performance mechanical and thermal insulating materials was successfully achieved by producing graphene/chitosan biocomposite aerogels through a straightforward, sustainable, and eco-friendly synthesis approach. The incorporation of graphene resulted in ultra-lightweight biocomposite aerogels with a 3D network structure showing an interconnected pore structure. This enhanced structure was attributed to the synergistic effects of attractive electrostatic interactions between positively charged chitosan and negatively charged graphene, as well as the formation of hydrogen bonds involving their hydroxyl and amino/acetamido groups. The present investigation highlighted the crucial effect of the preparation procedure in designing composite aerogels with improved mechanical performance. SEM images revealed that both the morphology and pore sizes of G-CS aerogels, along with their physical properties, could be tuned by varying the graphene content and the freezing temperature. The G_{10}-CS biocomposite aerogel, as fabricated at -60°C, exhibited the smallest pores (with an average diameter of approximately 76 µm), the highest Young's modulus (376 kPa), and the lowest thermal conductivity (0.038 $W.m^{-1}.K^{-1}$). Additionally, the G-CS composite aerogels displayed promising flame-retardant properties.

In summary, incorporating a small amount of graphene into biocomposite aerogels enhances their mechanical strength while preserving their thermal insulation, making them ideal for applications that require a balance of lightweight properties, mechanical robustness, and low thermal conductivity.

Notes

The authors declare no competing financial interest.

ACKNOWLEDGEMENTS

The authors gratefully acknowledge financial support from the French government grant administered by ANR as part of the national program of Investments for the Future for LabEx MMCD (ANR-11-LABX-022). The authors would also like to express their gratitude to R. Pires Brazuna for performing SEM analyses and to L. Michely for providing valuable guidance on mechanical measurements.

REFERENCES

1. Tettey UYA, Dodoo A, Gustavsson L. Effects of different insulation materials on primary energy and CO2 emission of a multi-storey residential building. Energy Build. 2014;82:369–377.
2. Koebel MM, Manz H, Emanuel Mayerhofer K, Keller B. Service-life limitations in vacuum glazing: A transient pressure balance model. Sol Energy Mater Sol Cells. 2010;94:1015–1024.
3. Koebel MM, Huber L, Zhao S, Malfait WJ. Breakthroughs in cost-effective, scalable production of superinsulating, ambient-dried silica aerogel and silica-biopolymer hybrid aerogels: from laboratory to pilot scale. J Sol-Gel Sci Technol. 2016;79:308–318.

4. Amaral-Labat G, Grishechko L, Szczurek A, Fierro V, Pizzi A, Kuznetsov B, et al. Highly mesoporous organic aerogels derived from soy and tannin. Green Chem. 2012;14:3099–3106.
5. Zuo L, Zhang Y, Zhang L, Miao Y-E, Fan W, Liu T. Polymer/Carbon-Based Hybrid Aerogels: Preparation, Properties and Applications. Materials. 2015;8:6806–6848.
6. Randall JP, Meador MAB, Jana SC. Tailoring Mechanical Properties of Aerogels for Aerospace Applications. ACS Appl Mater Interfaces. 2011;3:613–626.
7. Mao J, Iocozzia J, Huang J, Meng K, Lai Y, Lin Z. Graphene aerogels for efficient energy storage and conversion. Energy Environ Sci. 2018;11:772–799.
8. Gao L, Fan R, Zhou W, Hu X, Cao K, Wang W, et al. Biomimetic and Radially Symmetric Graphene Aerogel for Flexible Electronics. Adv Electron Mater. 2019;5:1900353.
9. Gupta S, Sharma SK, Pradhan D, Tai N-H. Ultra-light 3D reduced graphene oxide aerogels decorated with cobalt ferrite and zinc oxide perform excellent electromagnetic interference shielding effectiveness. Compos Part Appl Sci Manuf. 2019;123:232–241.
10. Bidgoli H, Mortazavi Y, Khodadadi AA. A functionalized nano-structured cellulosic sorbent aerogel for oil spill cleanup: Synthesis and characterization. J Hazard Mater. 2019;366:229–239.
11. Maleki H. Recent advances in aerogels for environmental remediation applications: A review. Chem Eng J. 2016;300:98–118.
12. Fu Y, Li C, Cheng Y, He Y, Zhang W, Wei Q, et al. Biomass aerogel composite containing BaTiO3 nanoparticles and MXene for highly sensitive self-powered sensor and photothermal antibacterial applications. Compos Part Appl Sci Manuf. 2023;173:107663.
13. Ganobjak M, Brunner S, Wernery J. Aerogel materials for heritage buildings: Materials, properties and case studies. J Cult Herit. 2020;42:81–98.
14. Cha J, Kim S, Park K-W, Lee DR, Jo J-H, Kim S. Improvement of window thermal performance using aerogel insulation film for building energy saving. J Therm Anal Calorim. 2014;116:219–224.
15. Jin R, Zhou Z, Liu J, Shi B, Zhou N, Wang X, et al. Aerogels for Thermal Protection and Their Application in Aerospace. Gels. 2023;9:606.
16. Ren H, Wu D, Li J, Wu W. Thermal insulation characteristics of a lightweight, porous nanomaterial in high-temperature environments. Mater Des. 2018;140:376–386.
17. Kerche EF, Lazzari LK, de Bortoli BF, de Oliveira Polkowski RD, de Albuquerque RFC. A systematic review of enhanced polyurethane foam composites modified with graphene for automotive industry. Graphene 2D Mater. 2024;9:27–46.
18. Li D, Lu Z, Ke Z, Xu K, Dai F, Yu Y, et al. Moisture resistant polyimide aerogel membranes with low dielectric constant and super thermal insulation for electronic device under harsh environment. Polymer. 2024;290:126478.
19. Kurd F, Fathi M, Shahedi M, Soltanizadeh N. Aerogel composite based on cellulose nanofibril and poly vinyl alcohol as insulation for meat packaging. J Food Eng. 2024;367:111854.
20. Xia W, Qu C, Liang Z, Zhao B, Dai S, Qiu B, et al. High-Performance Energy Storage and Conversion Materials Derived from a Single Metal–Organic Framework/Graphene Aerogel Composite. Nano Lett. 2017;17:2788–2795.
21. Hebalkar N, Kollipara KS, Ananthan Y, Sudha MK. Nanoporous Aerogels for Defense and Aerospace Applications. In: Mahajan YR, Johnson R, editors. Handb. Adv. Ceram. Compos. Def. Secur. Aerosp. Energy Appl., Cham: Springer International Publishing; 2020. 121–163.
22. Greszta A, Krzemińska S, Bartkowiak G, Dąbrowska A. Development of high-insulating materials with aerogel for protective clothing applications – an overview. Int J Mater Res. 2021;112:164–172.
23. Kim CH, Youn HJ, Lee HL. Preparation of cross-linked cellulose nanofibril aerogel with water absorbency and shape recovery. Cellulose. 2015;22:3715–3724.
24. Cao M, Li S-L, Cheng J-B, Zhang A-N, Wang Y-Z, Zhao H-B. Fully bio-based, low fire-hazard and superelastic aerogel without hazardous cross-linkers for excellent thermal insulation and oil clean-up absorption. J Hazard Mater. 2021;403:123977.

25. Chandrasekaran S, Campbell PG, Baumann TF, Worsley MA. Nanocarbons: Diamond, Fullerene, Nanotube, Graphite, and Graphene Aerogels. In: Aegerter MA, Leventis N, Koebel M, Steiner III SA, editors. Springer Handb. Aerogels, Cham: Springer International Publishing; 2023. p. 941–970.
26. Kistler SS, Caldwell AG. Thermal Conductivity of Silica Aërogel. Ind Eng Chem. 1934;26:658–662.
27. Schultz J, Jensen K, Kristiansen F. Super insulating aerogel glazing. Sol Energy Mater Sol Cells. 2005;89:275–285.
28. Bhuiya MMH, Anderson AM, Carroll MK, Bruno BA, Ventrella JL, Silberman B, et al. Preparation of Monolithic Silica Aerogel for Fenestration Applications: Scaling up, Reducing Cycle Time, and Improving Performance. Ind Eng Chem Res. 2016;55:6971–6981.
29. Zinzi M, Rossi G, Anderson AM, Carroll MK, Moretti E, Buratti C. Optical and visual experimental characterization of a glazing system with monolithic silica aerogel. Sol Energy. 2019;183:30–39.
30. Abbass A, Paiva MC, Oliveira DV, Lourenço PB, Fangueiro R. Graphene/polyurethane nanocomposite coatings – Enhancing the mechanical properties and environmental resistance of natural fibers for masonry retrofitting. Compos Part Appl Sci Manuf. 2023;166:107379.
31. Mahouche-Chergui S, Oun A, Haddadou I, Hoyez C, Michely L, Ouellet-Plamondon C, et al. Efficient and Recyclable Heterogeneous Catalyst Based on PdNPs Stabilized on a Green-Synthesized Graphene-like Nanomaterial: Effect of Surface Functionalization. ACS Appl Mater Interfaces. 2021;13:44673–44685.
32. Nassar G, Daou E, Najjar R, Bassil M, Habchi R. A review on the current research on graphene-based aerogels and their applications. Carbon Trends. 2021;4:100065.
33. Zhi D, Li T, Li J, Ren H, Meng F. A review of three-dimensional graphene-based aerogels: Synthesis, structure and application for microwave absorption. Compos Part B Eng. 2021;211:108642.
34. Saravanan N, Rajasekar R, Mahalakshmi S, Sathishkumar T, Sasikumar K, Sahoo S. Graphene and modified graphene-based polymer nanocomposites – A review. J Reinf Plast Compos. 2014;33:1158–1170.
35. Deshmukh K, Ahamed MB, Deshmukh RR, Pasha SKK, Sadasivuni KK, Ponnamma D, et al. Striking multiple synergies in novel three-phase fluoropolymer nanocomposites by combining titanium dioxide and graphene oxide as hybrid fillers. 2017. 2017. https://doi.org/10.1007/s10854-016-5559-1.
36. Zhang X, Yang G, Zong L, Jiang M, Song Z, Ma C, et al. Tough, Ultralight, and Water-Adhesive Graphene/Natural Rubber Latex Hybrid Aerogel with Sandwichlike Cell Wall and Biomimetic Rose-Petal-Like Surface. ACS Appl Mater Interfaces. 2020;12:1378–1386.
37. Wang Z, Liu L, Zhang Y, Huang Y, Liu J, Zhang X, et al. A Review of Graphene-Based Materials/Polymer Composite Aerogels. Polymers. 2023;15:1888.
38. Hsan N, Dutta PK, Kumar S, Koh J. Arginine containing chitosan-graphene oxide aerogels for highly efficient carbon capture and fixation. J CO_2 Util. 2022;59:101958.
39. Guo Q, Amendola E, Lavorgna M, Li Z, Feng H, Wu Y, et al. Robust and recyclable graphene/chitosan composite aerogel microspheres for adsorption of oil pollutants from water. Carbohydr Polym. 2022;290:119416.
40. Anouar A, Katir N, El Kadib A, Primo A, García H. Palladium Supported on Porous Chitosan–Graphene Oxide Aerogels as Highly Efficient Catalysts for Hydrogen Generation from Formate. Molecules. 2019;24:3290.
41. Wang R, Shou D, Lv O, Kong Y, Deng L, Shen J. pH-Controlled drug delivery with hybrid aerogel of chitosan, carboxymethyl cellulose and graphene oxide as the carrier. Int J Biol Macromol. 2017;103:248–253.
42. Chen J, Li H, Ma L, Jiang G, Li D, Wu Y, et al. Chitosan-based recyclable composite aerogels for the photocatalytic degradation of rhodamine B. Carbohydr Polym. 2021;273:118559.
43. Hao P, Zhao Z, Leng Y, Tian J, Sang Y, Boughton RI, et al. Graphene-based nitrogen self-doped hierarchical porous carbon aerogels derived from chitosan for high performance supercapacitors. Nano Energy. 2015;15:9–23.

44. Figueroa T, Carmona S, Guajardo S, Borges J, Aguayo C, Fernández K. Synthesis and characterization of graphene oxide chitosan aerogels reinforced with flavan-3-ols as hemostatic agents. Colloids Surf B Biointerfaces. 2021;197:111398.
45. Sehaqui H, Zhou Q, Berglund LA. High-porosity aerogels of high specific surface area prepared from nanofibrillated cellulose (NFC). Compos Sci Technol. 2011;71:1593–1599.
46. Ha H, Shanmuganathan K, Ellison CJ. Mechanically Stable Thermally Crosslinked Poly(acrylic acid)/Reduced Graphene Oxide Aerogels. ACS Appl Mater Interfaces. 2015;7:6220–6229.
47. Robertson J. Properties of diamond-like carbon. Surf Coat Technol. 1992;50:185–203.
48. Takeshita S, Sadeghpour A, Malfait WJ, Konishi A, Otake K, Yoda S. Formation of Nanofibrous Structure in Biopolymer Aerogel during Supercritical CO $_2$ Processing: The Case of Chitosan Aerogel. Biomacromolecules. 2019; 20:2051–2057.
49. Paraskevopoulou P, Gurikov P, Raptopoulos G, Chriti D, Papastergiou M, Kypritidou Z, et al. Strategies toward catalytic biopolymers: Incorporation of tungsten in alginate aerogels. Polyhedron. 2018;154:209–216.
50. Jiménez-Saelices C, Seantier B, Cathala B, Grohens Y. Spray freeze-dried nanofibrillated cellulose aerogels with thermal superinsulating properties. Carbohydr Polym. 2017;157:105–113.
51. Lee SK, Wang M, Lee JH, Suhr J. Development of reversibly compressible feather-like lightweight Chitosan/GO composite foams and their mechanical and viscoelastic properties. Carbon. 2020;157:191–200.
52. Mohod AV. Ultrasonic degradation of polymers: Effect of operating parameters and intensification using additives for carboxymethyl cellulose (CMC) and polyvinyl alcohol (PVA). Ultrason Sonochem. 2011:8.
53. Kasaai MR, Arul J, Charlet G. Fragmentation of chitosan by ultrasonic irradiation. Ultrason Sonochem. 2008:8.
54. Salzano de Luna M, Castaldo R, Altobelli R, Gioiella L, Filippone G, Gentile G, et al. Chitosan hydrogels embedding hyper-crosslinked polymer particles as reusable broad-spectrum adsorbents for dye removal. Carbohydr Polym. 2017;177:347–354.
55. Salzano de Luna M, Greco F, Pastore R, Mensitieri G, Filippone G, Aprea P, et al. Tailoring Chitosan/LTA Zeolite Hybrid Aerogels for Anionic and Cationic Dye Adsorption. Int J Mol Sci. 2021;22:5535.
56. Hu J, Zhu J, Ge S, Jiang C, Guo T, Peng T, et al. Biocompatible, hydrophobic and resilience graphene/chitosan composite aerogel for efficient oil−water separation. Surf Coat Technol. 2020;385:125361.
57. Chu K, Jia C. Enhanced strength in bulk graphene-copper composites: Enhanced strength in bulk graphene-copper composites. Phys Status Solidi A. 2014;211:184–190.
58. Senthil Kumar MS, Pon Selvan C, Sampath PS, Raja K, Nair R. Enhanced Mechanical Properties of Glass Fiber/Epoxy Composites using Nanoclay. 2019 Adv. Sci. Eng. Technol. Int. Conf. ASET, Dubai, United Arab Emirates: IEEE; 2019; 1–9.
59. Vo V-S, Mahouche-Chergui S, Nguyen V-H, Naili S, Carbonnier B. Crucial Role of Covalent Surface Functionalization of Clay Nanofillers on Improvement of the Mechanical Properties of Bioepoxy Resin. ACS Sustain Chem Eng. 2019;7:15211–15220.
60. Shao G, Hanaor DAH, Shen X, Gurlo A. Freeze Casting: From Low-Dimensional Building Blocks to Aligned Porous Structures—A Review of Novel Materials, Methods, and Applications. Adv Mater. 2020;32:1907176.
61. Zhang Y, Zhang L, Zhang G, Li H. Naturally Dried Graphene-Based Nanocomposite Aerogels with Exceptional Elasticity and High Electrical Conductivity. ACS Appl Mater Interfaces. 2018;10:21565–21572.
62. Li Z, Song X, Cui S, Jiao Y, Zhou C. Fabrication of macroporous reduced graphene oxide composite aerogels reinforced with chitosan for high bilirubin adsorption. RSC Adv. 2018;8:8338–8348.

63. Mi H-Y, Jing X, Politowicz AL, Chen E, Huang H-X, Turng L-S. Highly compressible ultra-light anisotropic cellulose/graphene aerogel fabricated by bidirectional freeze drying for selective oil absorption. Carbon. 2018;132:199–209.
64. Zhang M, Jiang S, Han F, Li M, Wang N, Liu L. Anisotropic cellulose nanofiber/chitosan aerogel with thermal management and oil absorption properties. Carbohydr Polym. 2021; 264:118033.
65. Sun Y, Chu Y, Deng C, Xiao H, Wu W. High-strength and superamphiphobic chitosan-based aerogels for thermal insulation and flame retardant applications. Colloids Surf Physicochem Eng Asp. 2022;651:129663.
66. Chen J, Xie H, Lai X, Li H, Gao J, Zeng X. An ultrasensitive fire-warning chitosan/montmorillonite/carbon nanotube composite aerogel with high fire-resistance. Chem Eng J. 2020;399:125729.
67. Zhu J, Zhao F, Xiong R, Peng T, Ma Y, Hu J, et al. Thermal insulation and flame retardancy of attapulgite reinforced gelatin-based composite aerogel with enhanced strength properties. Compos Part Appl Sci Manuf. 2020;138:106040.
68. Tang L, Zhuang S, Hong B, Cai Z, Chen Y, Huang B. Synthesis of light weight, high strength biomass-derived composite aerogels with low thermal conductivities. Cellulose. 2019;26:8699–8712.
69. Maleki H, Montes S, Hayati-Roodbari N, Putz F, Huesing N. Compressible, Thermally Insulating, and Fire Retardant Aerogels through Self-Assembling Silk Fibroin Biopolymers Inside a Silica Structure-An Approach towards 3D Printing of Aerogels. ACS Appl Mater Interfaces. 2018;10:22718–22730.
70. Wang X, Zhang H, Jana SC. Sulfonated syndiotactic polystyrene aerogels: properties and applications. J Mater Chem A. 2013;1:13989–13999.

Graphical abstract